# Optical characterization of deep-level defects in n-type Al$_x$In$_y$Ga$_{1-x-y}$P for the development of solid-state photomultiplier analogs

Andrew M Armstrong, Evan M Anderson*, Lisa N Caravello, Eduardo Garcia, Joseph P Klesko, Samuel D Hawkins, Eric A Shaner, John F Klem and Aaron J Muhowski

Sandia National Laboratories, Albuquerque, NM, United States of America

E-mail: emander@sandia.gov, aarmstr@sandia.gov and ajmuhow@sandia.gov

## Abstract

Characterizing intrinsic defects is an essential step in evaluating materials for novel optoelectronic device applications. For photomultipliers, suppressing dark currents is critical, but a tradeoff is present between maximizing the band gap while remaining sensitive to the wavelength of interest and minimizing the incorporation of fresh defects by growing not-yet-optimized alloys. We present a series of capacitance-based measurements, including deep-level optical spectroscopy, steady-state photocapacitance, and illuminated capacitance-voltage, on photodiodes with lightly *n*-type Al$_x$In$_y$Ga$_{1-x-y}$P absorber regions. Several deep levels are identified, including one near the midgap. Although the inclusion of aluminum increases each trap density by approximately $10\times$, the hole capture cross-section also appears to decrease, suggesting that Shockley–Read–Hall dark currents may be suppressed. These materials may be good candidates for the development into silicon photomultiplier analogs with a wider bandgap for scintillator applications.

Supplementary material for this article is available online

Keywords: deep level optical spectroscopy, photocapacitance, defect states, III–V, phosphides, photodiode

## 1. Introduction

Silicon photomultipliers (SiPMs) have been extensively investigated as a replacement for photomultiplier tubes (PMTs) in scintillation-based detection architectures [1–9].

Unlike vacuum tube–based PMTs, SiPMs are highly manufacturable, compact devices that benefit from decades of investment into silicon semiconductor fabrication processes. Despite these advantages, PMTs exhibit orders of magnitude lower dark count rates than SiPMs, which, as semiconductor devices, have additional dark current mechanisms that can trigger dark counts, such as generation-recombination (GR) and diffusion dark current. In order for SiPMs or SiPM-like devices to compete with PMTs in high-performance scintillators, such dark currents must be significantly reduced.

SiPMs comprise an array of Geiger-mode avalanche photodiodes; the dark current processes in an individual photodiode depend exponentially on the bandgap of the constituent

---

* Author to whom any correspondence should be addressed.

semiconductor. Diffusion dark current dominates in an ideal photodiode and can be expressed as follows:

$$J_{\text{diff}} = \frac{q\,n_i^2 w}{n_0 \tau_{\text{mc}}}$$

where $q$ is the elementary charge, $n_i$ is the intrinsic carrier density, $w$ indicates the lesser of either the minority carrier diffusion length or the width of the absorber region, $n_0$ represents the majority carrier density, and $\tau_{\text{mc}}$ is the minority carrier lifetime. In materials with short Shockley–Read–Hall lifetimes, the contribution from GR dark current can also be significant. The GR dark current density can be expressed as follows:

$$J_{\text{GR}} = \frac{q\,n_i w_{\text{dep}}}{\tau_{\text{mc}}}$$

where $w_{\text{dep}}$ is the width of the depletion layer. The intrinsic carrier density, which appears in both expressions, in turn depends on the bandgap ($E_{\text{g}}$) of the absorber material as follows:

$$n_i \propto \exp\left(-\frac{E_{\text{g}}}{2\,k_{\text{B}}T}\right).$$

Ideally, the largest possible bandgap that maintains appreciable optical absorption at the scintillator wavelength should be selected to suppress diffusion and GR dark current processes. However, such materials with smaller bandgaps may still be optimal if the minority carrier lifetime is considerably longer than another candidate material with a larger bandgap.

Semiconductor systems offer variability in the available bandgaps and technological maturity, both of which must be considered when identifying candidates for next-generation SiPM-like detectors. Consider the fluorescence photon energy from commonly used NaI(Tl) scintillators of 3 eV, for example, which precludes the use of wide-bandgap materials like GaN and 4 H-SiC, as they would not substantially absorb photons from the scintillator crystal [10, 11]. Among III–V materials, the alloy $Al_x Ga_{1-x}P$ has the widest bandgap that could mediate photodetection in a scintillator; however, the available GaP substrates are small, expensive, and burdened by high etch pit densities [12]. The $Al_x In_y Ga_{1-x-y}P$ system lattice-matched to widely available and mature GaAs substrates can provide nearly the same bandgap with high Al content, ranging from 1.9 to 2.4 eV—approximately twice that of Si. Although the increased bandgap suggests that dark processes may be reduced, such a reduction still requires the minority carrier lifetimes to be sufficiently long. General trends within III–V semiconductors imply that the inclusion of Al incurs an increase in oxygen incorporation and consequent point defect densities. At present, there is limited knowledge of minority carrier lifetimes and much less information on the deep levels that contribute to Shockley–Read–Hall recombination, which are attainable in low-doped $Al_x In_y Ga_{1-x-y}P$ candidate materials [13–15]. Nevertheless, avalanche photodiodes comprising InGaP, InAlP, and even SiPM-like devices have demonstrated promising performance, suggesting that further studies of $Al_x In_y Ga_{1-x-y}P$ are warranted [16–18].

Here, we present a deep-level optical spectroscopy (DLOS) study of photodiodes consisting of $In_{0.49}Ga_{0.51}P$ (InGaP hereafter) and $Al_{0.13}In_{0.48}Ga_{0.39}P$ (AlInGaP hereafter) absorber materials. Previous studies of deep-level defects in InGaP- or AlInGaP-based solar cells or light emitting diodes used deep-level transient spectroscopy (DLTS) [19–23]. However, DLTS is a thermally stimulated technique that is typically limited to observing deep levels that lie <1 eV from the band edge and thus might not be able to observe near-mid-gap deep levels in $Al_x In_y Ga_{1-x-y}P$ that could produce dark currents and limit minority carrier lifetimes. As an optically stimulated technique, DLOS is able to observe deep levels lying near-mid-gap in $Al_x In_y Ga_{1-x-y}P$. DLOS has been performed on InGaP- [24] and AlInGaP- [25] based solar cells, but III-P-based solar cells use *p*-type absorber regions, whereas the photodiodes in this study use *n*-type absorber layers. Deep-level defect incorporation is expected to differ for *n*- versus *p*-type AlInGaP alloys because the formation energy of native defects can depend strongly on the energetic position of the Fermi level. Thus, our DLOS study focusses on lightly doped *n*-type materials, which could be used in *p*–*ν*–*n* avalanche photodiodes. We identify three deep-level defects in both InGaP and AlInGaP, two of which have similar distances from the band edges and thermodynamic energies that suggest analogous atomistic origins of these defects for the two materials. We also observe deep-level density increasing by more than an order of magnitude with the inclusion of Al. Despite the high trap density, our study suggests that the hole capture cross-section may be significantly smaller in AlInGaP than in InGaP, potentially yielding a minority carrier lifetime, and thus a dark current, advantage for AlInGaP over InGaP.

## 2. Methods

Samples were grown by molecular beam epitaxy using a phosphine gas source and a solid-source arsenic cracker on *n*-type, (100) GaAs substrates. *n*- and *p*-type dopants were Si and Be, respectively. For both the InGaP and AlInGaP absorber materials under study here (figure 1), growth begins with a 100-nm *n*-GaAs buffer layer before lowering the growth temperature to 515°C for 100 nm of *n*-InGaP doped to $1 \times 10^{18}\,\text{cm}^{-3}$ followed by 900 nm of the absorber material. The first 100 nm were doped $1 \times 10^{18}\,\text{cm}^{-3}$ *n*-type, the next 700 nm $6 \times 10^{16}\,\text{cm}^{-3}$ *n*-type, and the final 100 nm $1 \times 10^{18}\,\text{cm}^{-3}$ *p*-type. From there, a 23-nm digital grade was grown to a *p*-type InAlP window layer at a doping of $1 \times 10^{18}\,\text{cm}^{-3}$. Finally, a heavily *p*-type InGaP and GaAs contact structure was grown.

Photodiodes were fabricated using standard photolithographic techniques (figure 2). First, mesas were reticulated by wet chemical etching through the arsenide and phosphide layers to the underlying substrate. The aqueous HCl or $HCl:H_3PO_4$ chemistry that is typically used to selectively etch phosphides over arsenides laterally etches Al-rich phosphides, namely the InAlP layer, much faster in <010> directions than in <011> directions and severely undercuts the mask [26]. This led to the development of a nonselective etch using aqueous $HNO_3:HCl$ to balance the slow etch rate with low
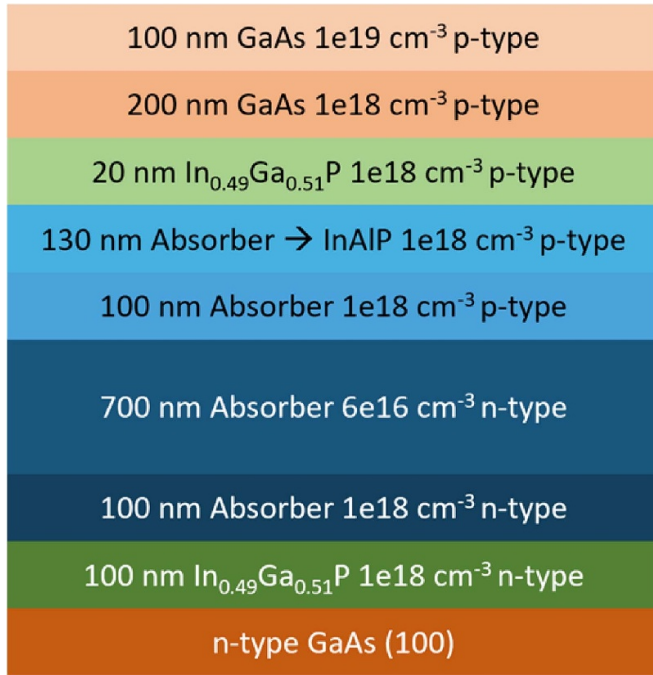
**Figure 1.** Schematic cross section of the epitaxial samples, where the absorber is either $In_{0.49}Ga_{0.51}P$ or $Al_{0.13}In_{0.48}Ga_{0.39}P$.

HCl concentration versus the anisotropic etching with high HCl concentration. The devices were then encapsulated in approximately 2000 Å of $Si_3N_4$ to provide electrical isolation between the semiconductor and offset bond pads. Next, vias were etched through $Si_3N_4$ via reactive ion etching to allow for ohmic contacts at the top of each diode. The top electrical contacts were patterned as an annulus to allow for an optical window for measurements. The metals for the *p*-type (top of diode) and *n*-type (back of wafer) electrical contacts, consisting of at least 20 nm of an adhesion layer and 200 nm of Au, were then deposited on the devices, followed by a 30 s rapid thermal anneal at 400 °C under argon flow. Finally, the GaAs layer was etched from the optical windows using the metal and remaining $Si_3N_4$ as a mask to prevent GaAs from interfering with the optical measurements of the underlying phosphide layers.

The photodiodes were characterized using dark and lighted current-voltage (*I*–*V*) and capacitance-voltage (*C*–*V*). All *C*–*V* and *I*–*V* measurements were performed at room temperature. The doping level in the absorber regions near the p-n junction was measured by *C*–*V*. The *C*–*V* data for both types of photodiodes, shown in figure 3, were collected using a 1 MHz frequency with a 30 mV ac amplitude. To extract the net doping ($n_0$) from *C-V* measurements, the physical mesa area (*A*) was used as the junction area for the diodes. Uncertainty in $n_0$ can be determined from the standard error propagation analysis of the usual equation relating $n_0$ and $C(V)$:

$$n_0 = \frac{C^3}{q \in A^2 \frac{dC}{dV}}.$$

where *A* is the junction area, *q* is the fundamental charge, and $\in$ is the dielectric permittivity in semiconductors. The
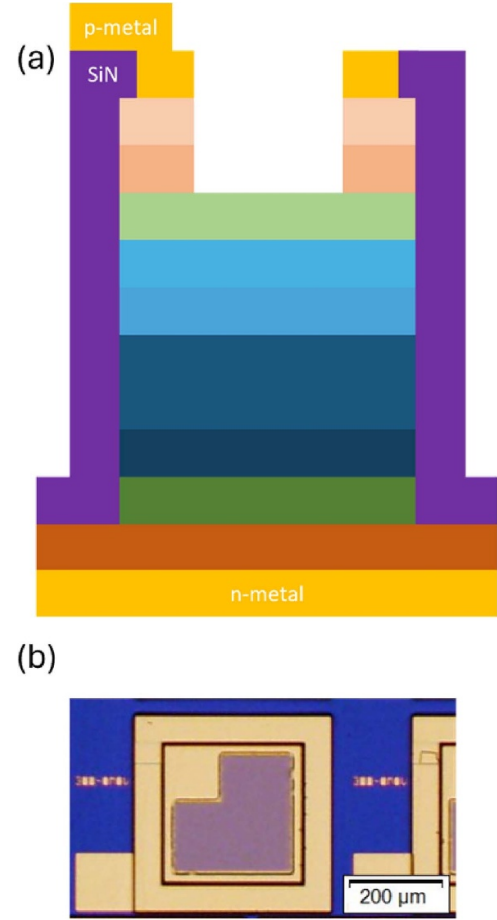


**Figure 2.** (a) Cross-sectional schematic of the fabricated photodiodes. (b) Optical image of a fabricated diode.
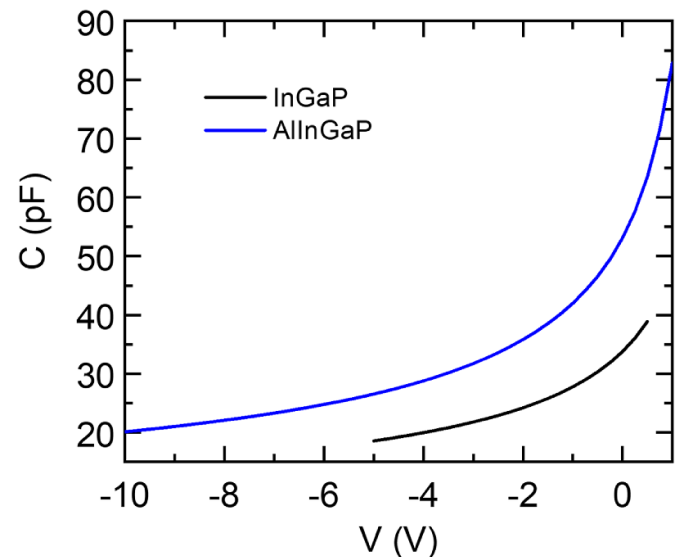


**Figure 3.** *C-V* data for the photodiodes.

square mesa sidewall length (nominally 300 $\mu$m) variation was assumed to be 2 $\mu$m because of photolithographic variations. This sidewall length uncertainty results in 0.9% uncertainty ($\sigma_A/A$). Mesa area uncertainty is expected to be the largest source of experimental errors for extracting doping

from $C$–$V$ measurements because the capacitance meter resolution is small (1 fF) compared to the junction capacitance (19–29 pF, depending on bias) and the voltage resolution was small (0.001 V) compared to the applied voltage ($\sim$−5 V), implying percentage errors of $C^3$ and $dC/dV \ll 1\%$. The extracted doping for a given $C(V)$ value then varied as $n_0 \sim k/A^2$, where $k$ is a constant with negligible uncertainty compared to $A$, so that the percentage error of $n_0$ ($\sigma_{n0}/n_0$) $\sim (2\sigma_A/A)^{1/2} = 1.3\%$. The extracted $n_0$ was $6.4 \times 10^{16}$ cm$^{-3}$ for the AlInGaP photodiode, and $n_0 = 3.4 \times 10^{16}$ cm$^{-3}$ for the InGaP photodiode. As explained in the Results and Discussion section below, lower doping in the InGaP photodiode resulted from lower-than-expected dopant incorporation rather than higher levels of dopant compensation by defects.

DLOS, steady-state photocapacitance (SSPC), and lighted capacitance–voltage (LCV) were used to examine and compare deep-level defect states for the two different alloys. DLOS, SSPC, and LCV measurements were performed at room temperature. DLOS determines the optical deep-level energy ($E^o$) relative to the majority carrier band edge (the conduction band in this case), whereas SSPC measures the deep-level concentration ($N_t$) when $N_t$ is uniform and much lower than the dopant concentration ($N_d$). For the cases when $N_t \sim N_d$ or when $N_t$ has a strong depth dependence, LCV can be used to measure $N_t$ [27, 28].

DLOS is a differential photocapacitance technique that uses monochromatic, subbandgap energy photons to measure the deep-level optical cross-section ($\sigma^o$) [29]. Fitting the line shape of $\sigma^o$ to a model [30, 31] determines $E^o$ and the Franck–Condon energy ($d_{FC}$). The authors selected the model of Pässler [31] because it is more parsimonious compared to the model of Chantre *et al* [29]. The Chantre model includes an ad hoc "$m$" fitting parameter that accounts for the degree of admixture between conduction- and valence-band-like states for the deep-level defect wave function, but this parameter has no direct, physical analog. In contrast, the Pässler model only includes the physical values of optical deep-level energy, Franck–Condon energy, and local vibrational phonon energy.

The optical deep-level energy is the minimum $hv$ required to delocalize a carrier from a deep-level defect into an energy band in the absence of any phononic interaction between the defect and the lattice. The Franck–Condon energy is the average vibronic energy of a localized carrier on a defect at a given temperature due to the phonon excitation of local breathing modes. The photon energy required to delocalize a carrier from a defect is reduced by $d_{FC}$; therefore, the average $hv$ required for the photoemission of a localized carrier from a defect is $E^o$–$d_{FC}$. At finite temperature, defects in the lattice have an ensemble of vibronic energies, which gives rise to the homogeneous broadening of $hv$ required to induce photoexcitation from a deep level. This manifests itself as a temperature-dependent broadening of the defect absorption spectrum, that is, $\sigma^o$. For the case of strong lattice coupling due to the defect, that is, strong electron-phonon interaction of a carrier localized on the defect. $E^o$ and $d_{FC}$ values can be extracted by fitting $\sigma^o$ to the model of Pässler [31], which uses an amplitude prefactor, the average defect breathing mode energy ($\varepsilon$), $E^o$, and $d_{FC}$ as variables. For the case of weak lattice coupling with the

defect, the resulting sharp $\sigma^o$ can be described by the model of Lucovsky [30] that uses only the amplitude prefactor and $E^o$ as variables. The model of Pässler reduces to the Lucovsky model for the case of $d_{FC} = 0$.

Deep level $\sigma^o$ was determined experimentally by measuring the photocapacitance transients $\Delta C(t)$ arising from deep-level defect photoemission upon exposure to monochromatic photons. For electron photoemission from deep-level defects located in an $n$-type depletion region, $\Delta C(t)$ is an exponential decay characterized by an optical emission rate [32] $e^{o,n}(hv) = \sigma^o(hv)\phi(hv)$, where $\phi$ is the incident photon flux. Thus, $\sigma^o$ is determined by measuring $\Delta C(t)$ at several $hv$ values and extracting $e^{o,n}$ from a least-squares fit (an example of $\Delta C(t)$ data and their fitting is shown in figure S1 in the Supplementary Material) and then normalizing to $\phi$. For positive (negative) $\Delta C$, $E^o$ is referenced to the majority (minority) carrier band edge. The experiment proceeded as follows. The diode was held in the dark at room temperature under a reverse measurement bias ($V_r$), and it was assumed that all deep-level defects in the depletion region were fully occupied. Monochromatic light was provided using a Xe arc lamp source filtered through a 1/4 m monochromator with mode-sorting filters to achieve monochromatic illumination with $\phi = 1 \times 10^{17}$ cm$^{-2}$ s$^{-1}$ that was held constant by adjusting the monochromator slit width. Variable slit width resulted in a monochromator energy resolution of $\sim$5 meV for $0.6 < hv < 1.5$ eV and 15–25 meV for $1.5 < hv < 2.4$ eV. A collimating lens and a focusing lens were used to produce an output beam from the monochromator that was approximately 1 mm $\times$ 3 mm. Photon flux was measured for each $hv$ using an optical power meter, accounting for the beam size. Diodes were illuminated through a top-side annular metal contact. DLOS was measured at a $V_r = -5$ V. After recording $\Delta C(t)$, an electrical fill pulse bias ($V_f$) $= +1$ V was applied to reduce the depletion region width and allow deep-level defects to thermally recapture carriers. The positive $V_f$ is below the diode turn-on voltage but still produces several hundred microamps of forward current that provide low-level hole injection into the $n$-regions of the $p^+$-$n$ diode. A 30-second delay between the end of the electrical fill pulse and the beginning of subsequent illumination allowed time for any thermal capacitance transient to decay before the optical excitation of deep level defects.

The above analysis relating $\sigma^o$ and $e^o$ is valid for photoemission of a single carrier type (electron or hole). However, for $hv$ greater than half the band gap energy, the simultaneous optical emission of both electrons and holes from a deep level can occur, giving $e^o = (e^{o,n} + e^{o,p})$ for $\Delta C(t)$. Determining $E^o$ requires separating $e^{o,n}$ and $e^{o,p}$. Since the SSPC $\Delta C_{ss} \propto e^{o,n}/(e^{o,n} + e^{o,p})$, $E^o$ can be determined from $\sigma^{o,n} = e^{o,n}/\phi \propto e^o \Delta C_{ss}/\phi$ [2].

SSPC and LCV are the methods used to determine $N_t$. Using SSPC, $N_t = 2n_0\Delta C_{ss}/C_0$, where $C_0$ is the capacitance in the dark. However, this expression for $N_t$ only holds for the case of small $\Delta C/C_0$, that is, small $N_t/n_0$. For the AlInGaP device, $\Delta C$ was comparable to $C_0$ and, thus, SSPC could not be used to measure $N_t$, so LCV was used instead. LCV measures $N_t$ from the difference of space-charge density profiles measured by $C$–$V$ under subband gap illumination.

Photon energies are chosen to selectively depopulate deep-level defects one at a time, and the increase in the space-charge density determined from *C*–*V* provides $N_t$ as a function of depth. For LCV, $N_t$ had an uncertainty:

$$\sigma_{N_t}(x_d) = \sqrt{\left[(\sigma_{n0}/n_0) * n_{h\nu 1}(x_d)\right]^2 + \left[(\sigma_{n0}/n_0) * n_{h\nu 2}(x_d)\right]^2}$$

where $x_d$ is the depletion depth, $n_{h\nu 1(2)}$ refers to the extracted doping value for photon energies $h\nu_1$ or $h\nu_2$ and the percentage uncertainty in $n_{h\nu 1(2)} = \sigma_{n0}/n_0$ for that of *C*–*V* measurements, as described above. An evaluation of $\sigma_{N_t}$ is provided in the Results and Discussion section below.

## 3. Results and discussion

Figure 4 illustrates the DLOS spectrum for the InGaP diode. Two deep levels with broad spectral line shapes were observed, and simultaneous fitting of both to the model of Pässler [31] determined $E^o = 1.06$ eV ($d_{FC} = 0.28$ eV) and $E^o = 1.58$ ($d_{FC} = 0.16$ eV), respectively. A third deep level with a sharp line shape was fit using the Lucovsky model [30] to determine $E^o = 1.81$ eV. Nonlinear least-squares regression fitting of the DLOS data in figure 4 to the model of Pässler [31] produced a root mean squared error (RMSE) of 0.05 eV. This value was taken to be the uncertainty for both $E^o$ and $d_{FC}$ values for the $E_c$–1.06 eV and $E_c$–1.58 eV deep levels. Nonlinear least-squares regression fitting of the DLOS data in figure 4 to the model of Lucovsky produced RMSE = 0.07 eV, which was taken to be the uncertainty for $E^o$ for the $E_c$–1.81 eV deep level. The DLOS spectrum saturates at the InGaP band gap energy of 1.90 eV as free carrier absorption, which creates a photocurrent rather than photocapacitance, begins to dominate. As shown below, $\Delta C$ for these deep levels are positive, indicating majority carrier emission in the conduction band; hence, their $E^o$ values are referenced to the conduction band minimum energy ($E_c$).

SSPC determined the concentration of the deep levels observed by DLOS and revealed the role of the $E_c$–1.06 eV deep level as a recombination center. The SSPC spectra in figure 5 display three positive changes in slope at 1.15, 1.55, and 1.80 eV, correlating to the onset of electron photoemission from the $E_c$–1.06 eV, $E_c$–1.58 eV, and $E_c$–1.81 eV deep levels, respectively. For each deep level, $\Delta C_{ss}/C_0$ is small; so, figure 5 shows the corresponding $N_t$ data. SSPC is a cumulative measurement; therefore, $N_t$ of the $E_c$–1.58 eV deep level is the change in net $N_t$ from 1.55 to 1.80 eV. Likewise, $N_t$ for the $E_c$–1.81 eV deep level is the change in net $N_t$ from 1.80 to 1.90 eV. The ascription of the SSPC signal between 1.80 and 1.90 eV to the $E_c$–1.81 eV agrees with the abrupt emergence of this deep level at 1.80 eV in the $\sigma^o$ spectrum of figure 4. Partitioning of the SSPC signal from the $E_c$–1.58 eV level with broader $\sigma^o$ is ambiguous because it lacks an abrupt absorption threshold in figure 4. In this case, 1.55 eV was selected as the demarcation in the SSPC signal onset for the $E_c$–1.58 eV deep level based on the deviation from a horizontal line guide to the eye. Note that the SSPC signal near 1.50 eV is slowly varying; hence, the assignment of SSPC demarcation energy in this region does not exert a significant impact on $N_t$.
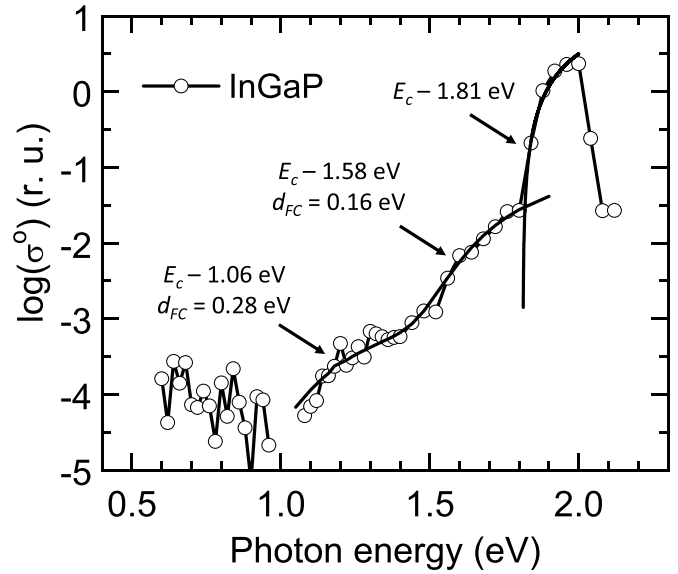


**Figure 4.** DLOS spectrum of the InGaP diode. The symbols are experimental data and the curves are fits to the Pässler model [31] for the $E_c$–1.06 eV and $E_c$–1.58 eV levels and the Lucovsky [30] model for the $E_c$–1.81 eV level. The scatter in the data for $h\nu < 1$ eV indicates the noise floor of the measurement where no deep levels were observed.
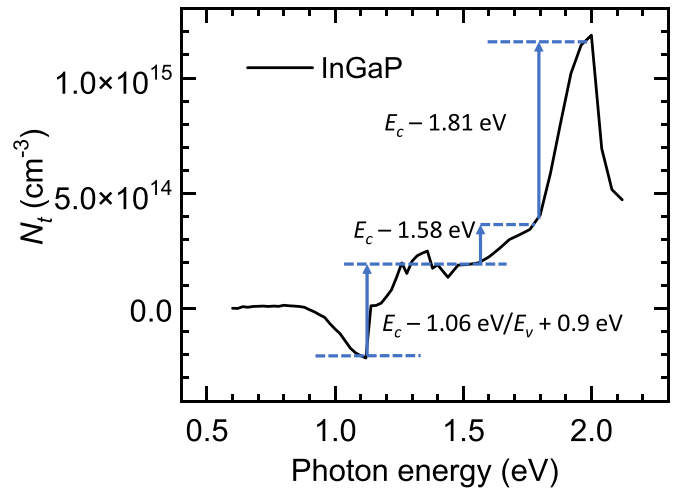


**Figure 5.** SSPC spectrum of the InGaP diode. The arrows indicate how the total deep level concentration was apportioned among the individual deep levels.

The analysis of $N_t$ for the $E_c$–1.06 eV deep level is more involved because its positive $\Delta C_{ss}$ is preceded by a negative threshold at 0.9 eV. Negative SSPC indicates minority carrier photoemission, in this case, holes to the valence band maximum $E_v$. Thus, the physical interpretation of negative $N_t$ in figure 5 is the concentration of holes thermally captured by the deep-level defect during the electrical fill pulse and subsequently photoemitted to the valence band during illumination. DLOS for the negative $\Delta C(t)$ was not resolved well enough to determine $E^o$ accurately for hole photoemission from the deep level, but $E^o$ can be approximated as $h\nu$ where

$\Delta C$ (and thus $N_t$) becomes negative, placing the corresponding deep level at approximately $E_v + 0.9$ eV. The fact that the $E_v + 0.9$ eV and $E_c{-}1.06$ eV deep level energies sum approximately to the band gap energy and that the transition between their corresponding negative and positive SSPC features is very abrupt suggests that these two deep levels are at the same deep level with $e^{o,p} \gg e^{o,n}$ for $hv < 1.10$ eV and $e^{o,n} \gg e^{o,p}$ for $hv > 1.15$ eV. This $E_c{-}1.06$ eV/$E_v + 0.9$ eV deep level is likely to be an effective recombination center because it can thermally capture carriers from both the conduction and valence bands during the electrical fill pulse to produce both electron and hole photoemission. That is, this level is normally unoccupied and can efficiently capture both electrons and holes that have been generated either electrically or optically. The concentration of the $E_c{-}1.06$ eV/$E_v + 0.9$ eV deep level was calculated as the change in net $N_t$ from $hv = 1.15$ eV (when the level is most occupied by electrons) to $hv = 1.50$ eV (when the level is least occupied).

Comparing the DLOS/SSPC spectra for *n*-InGaP photodetectors studied here with previous DLOS [24] and DLTS [19] studies of *p*-InGaP base regions of solar cells provides insight into possible atomistic sources of the observed deep levels. Previous DLOS and DLTS of as-grown, *p*-InGaP [19, 24] did not observe deep levels consistent with those reported here for *n*-InGaP. However, proton irradiation of *p*-InGaP produced a deep level at $E_v + 0.9$ eV that was found to readily capture carriers from both the conduction and valence band [19]. It is concluded that the *p*-InGaP $E_v + 0.9$ eV and the *n*-InGaP $E_c{-}1.06$/$E_v + 0.9$ eV deep levels are likely the same defects based on their similar energy and ability to thermally interact with both the valence and conduction bands. Thermal annealing investigations attributed the *p*-InGaP $E_v + 0.9$ eV deep level to a phosphorus vacancy or a related antisite [19].

DLOS and SSPC spectra were measured for the AlInGaP sample to compare to that of InGaP and are shown in figures 4 and 5, respectively. AlInGaP has a band gap of 2.04 eV, as determined through photoluminescence. The DLOS spectrum for AlInGaP has qualitative similarities to that of InGaP, including a near-$E_v$ deep level at $E_c{-}1.97$ eV (fit using the Lucovsky model [30]), a deep level at the lower third of the band gap at $E_c{-}1.80$ eV with $d_{FC} = 0.43$ eV (fit using the Pässler model [31]), and a broad line-shape around the middle of the band gap energy. It is noted that the InGaP and AlInGaP DLOS spectra both exhibit deep levels with $E^o$ near 1.8 eV; however, these deep levels are not likely related. The InGaP $E_c{-}1.81$ eV deep level with $d_{FC} = 0$ eV has a sharp $\sigma^o$ consistent with an effective-mass-like state with weak lattice coupling, while the AlInGaP $E_c{-}1.80$ eV deep level with $d_{FC} = 0.43$ eV has a broad $\sigma^o$ consistent with a highly localized state with strong lattice coupling. Nonlinear least-squares regression fitting of the DLOS data in figure 6 to the model of Pässler [31] produced an RMSE of 0.02 eV. This value was taken to be the uncertainty for both $E^o$ and $d_{FC}$ values for the $E_c{-}1.80$ eV deep level. Nonlinear least-squares regression fitting of the DLOS data in figure 6 to the model of Lucovsky produced an RMSE = 0.01 eV, which was taken to be the uncertainty for $E^o$ for the $E_c{-}1.97$ eV deep level. The AlInGaP $E_c{-}1.97$ eV and the InGaP $E_c{-}1.81$ eV deep levels have nearly
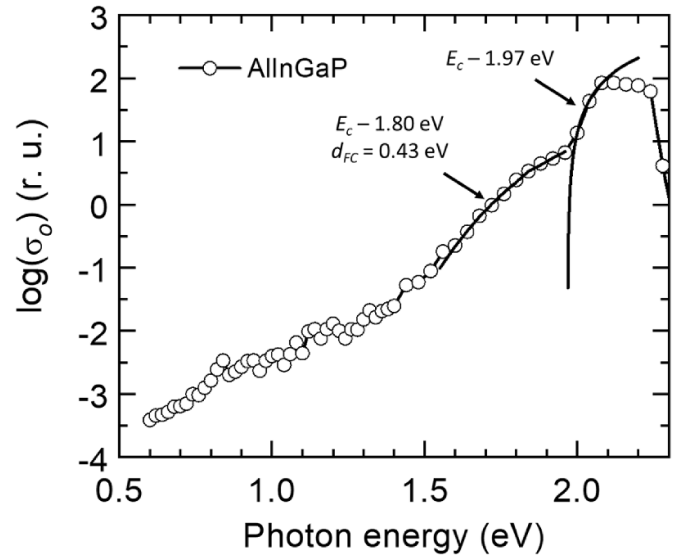


**Figure 6.** DLOS spectrum of the AlInGaP diode. The symbols are experimental data and the curves are fits to the Pässler model [31] for the $E_c{-}1.80$ eV level and the Lucovsky model [30] for the $E_c{-}1.97$ eV level. The line-shape at 0.60–1.50 eV was too broad to be well fit.

the same energy relative to their respective $E_v$, which suggests that they might have a similar atomistic source whose electronic structure is primarily derived from the valence band and thus tends to track $E_v$ with alloying [33].

For defect states energetically located far from a band edge, the vacuum-referred binding energy (VRBE) model has been used among related compound semiconductors [33] and their alloys [34] to assess if they share a common atomistic source. In the VRBE model, a defect within a family of semiconductors is expected to form at an energy level $E_{vac}{-}\chi{-}E_{th}$, where $E_{vac}$ is the vacuum level, $\chi$ is the electron affinity and $E_{th} = E^o{-}d_{FC}$ is the thermodynamic energy level. The electron affinity for InGaP and AlInP alloys latticed-matched to GaAs only differs by approximately 0.1 eV [35]; hence, it is reasonable to assume that $\chi$ for the alloys studied here are similarly close. In this case, comparing $E_{th}$ is a good proxy for the VRBE model. The AlInGaP $E_c{-}1.80$ eV deep level has $E_{th} = 1.37$ eV and the InGaP $E_c{-}1.58$ eV level has $E_{th} = 1.42$ eV. Thus, attributing these deep levels to the same atomistic source is consistent with the VRBE model; however, the atomistic source remains unknown. The difference in $d_{FC}$ for the $E_c{-}1.80$ eV and $E_c{-}1.58$ eV deep levels accounts for how their $E_{th}$ values can be similar despite very different $E^o$ values. The large $d_{FC}$ for the $E_c{-}1.80$ eV deep level indicates that, upon photoemission of a carrier, the change in local electronic bonding around the corresponding AlInGaP defect center induces a drastic spatial reconfiguration of the nearby atoms that releases substantial mechanical energy via phonon emission. The smaller $d_{FC}$ for the $E_c{-}1.58$ eV InGaP deep level suggests that the atomic reconfiguration around the corresponding defect center in InGaP is much less drastic and energetic after electron photoemission. One possible explanation of this scenario is that inclusion of Al in the matrix leads to a more
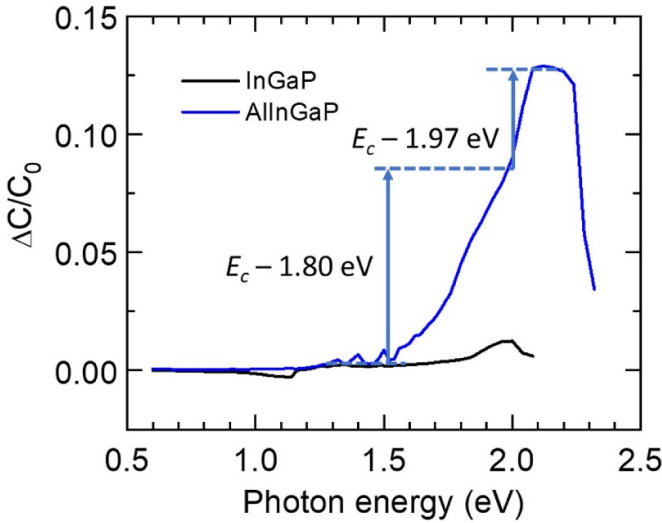
**Figure 7.** SSPC spectra of the InGaP and AlInGaP diodes. The InGaP data correspond to those in figure 4 but are recast as the relative change in photocapacitance. The arrows indicate $\Delta C/C_0$ of individual deep levels for the AlInGaP diode.
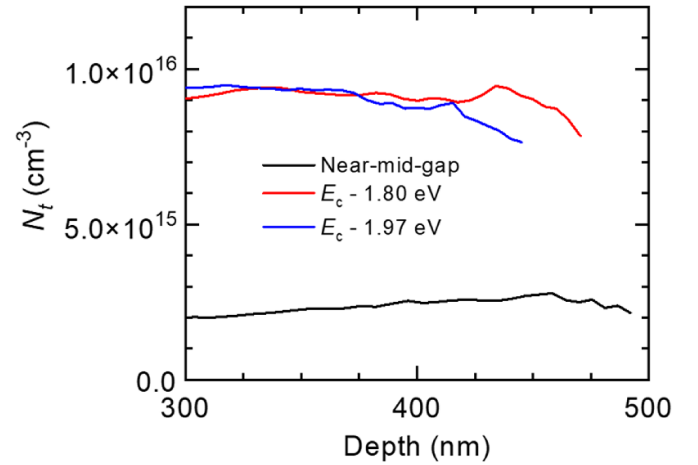


**Figure 8.** LCV data for the AlInGaP diode showing $N_t$ profiles determined from differencing the space-charge profiles shown in the inset of figure 9.

**Table 1.** Deep level concentrations for both alloys.

| InGaP | | AlInGaP | |
|---|---|---|---|
| Energy (eV) | $N_t$ (cm$^{-3}$) | Energy (eV) | $N_t$ (cm$^{-3}$) |
| $E_c$–1.06/$E_v$ + 0.9 | $4.0 \times 10^{14}$ | Near-mid-gap | $2.3 \times 10^{15}$ |
| $E_c$–1.58 | $1.5 \times 10^{14}$ | $E_c$–1.80 | $9.3 \times 10^{15}$ |
| $E_c$–1.81 | $8.2 \times 10^{14}$ | $E_c$–1.97 | $9.3 \times 10^{15}$ |

"crowded' atomic configuration around the defect center, and thus a more "rigid" coupling between local atoms and thereby a more energetic relaxation process when the local bonding is disrupted upon delocalization of a bound electron through photoemission.

The $\sigma^o$ line shape for AlInGaP around the middle of the band gap indicates the presence of a near-mid-gap deep level. However, this line shape is too broad to be well fit with the Pässler model, so $E^o$ and $d_{FC}$ could not be determined. Nonetheless, SSPC reveals significant differences between the near-mid-gap deep levels of the InGaP and AlInGaP diodes.

The SSPC spectra in figure 7 reveal two stark differences in the deep level spectra of InGaP and AlInGaP. First, the AlInGaP near-mid-gap deep level does not exhibit hole photoemission, i.e. negative $\Delta C$. This observation implies that the thermal hole capture cross-section for the AlInGaP near-mid-gap deep level is much smaller than the InGaP $E_c$–1.05 eV deep level. A much lower thermal hole capture cross-section for the mid-band gap deep level in the AlInGaP versus InGaP alloy would make the former a much less effective nonradiative recombination center. The second major difference revealed by the SSPC spectra in figure 7 is that the AlInGaP has a much larger overall $\Delta C/C_0$, i.e. $N_t/N_d$, compared to the InGaP diode. Indeed, $\Delta C/C_0$ for the AlInGaP diode was so large that the LCV was used to determine $N_t$. The spatial profiles for the AlInGaP deep levels are shown in figure 8. Table 1 lists $N_t$ data for the deep levels of both alloy compositions. Since $n_{h\nu}$ were approximately constant with $x_d$, the typical $\sigma_{Nt}/N_t$ values for the data in figure 9 were 1.2, 1.3 and $1.5 \times 10^{15}$ cm$^{-3}$ for the near-mid-gap, $E_c$–1.80 eV and $E_c$–1.97 eV deep levels, respectively. LCV was not performed for the InGaP diode because its $\sim 10^{15}$ cm$^{-3}$ uncertainty in $N_t$ was larger than $N_t$ values $\sim 10^{14}$ cm$^{-3}$ determined from the SSPC. A comparison of these data to the net dopant concentration $N_d^* = N_d - \Sigma N_t$ measured by C–V (assuming all observed deep
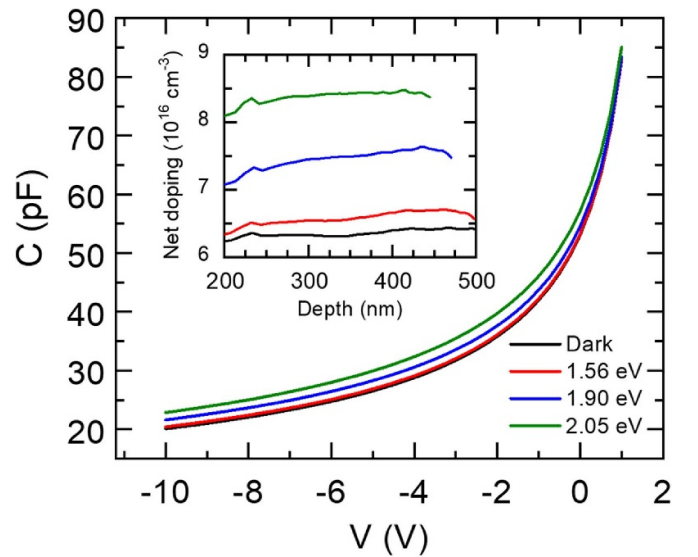


**Figure 9.** LCV data for the AlInGaP photodiode and extracted space-charge profiles under illumination (inset).

levels are acceptor-like) shows that the InGaP diode was subject to only 4% compensation compared to 25% compensation for the AlInGaP diode. Thus, the AlInGaP alloy poses a doping challenge due to a high deep-level concentration but might nonetheless have longer minority carrier lifetime, and thus lower dark current, due to reduced thermal hole capture by mid-gap deep levels compared to the InGaP alloy.

## 4. Conclusions

We have examined the defect characteristics of lightly doped *n*-type InGaP and AlInGaP alloys using several capacitance-based measurement techniques. Our analysis reveals the presence of several deep-level traps, with one in particular near the midgap. The deepest optically identified defect energies in each material, $E_c-1.97$ eV and $E_c-1.80$ eV for AlInGaP and $E_c-1.81$ eV and $E_c-1.58$ eV for InGaP, have similar thermodynamic energies and distances from the band edges, suggesting analogous, though not identified, atomistic origins for these defects between the two materials. The inclusion of Al increases the density of the observed trap states by approximately an order of magnitude; however, the midgap state appears to have a reduced hole capture the cross-section in AlInGaP compared to InGaP and may thus be less efficient at mediating the generation of dark current. Our results suggest that the InGaP and AlInGaP materials may be good candidates for the development of SiPM-like devices optimized for shorter wavelengths and lower dark count rate scintillator systems.

## Data availability statement

The data that support the findings of this study are available from the corresponding author upon reasonable request.

DLOS capacitive transient fit available at https://doi.org/10.1088/1361-6641/ae1b37/data1.

## Acknowledgments

## Author contributions

Andrew M Armstrong 0000-0003-0391-6009
Data curation (equal), Formal analysis (lead), Investigation (equal), Methodology (equal), Writing – original draft (equal), Writing – review & editing (equal)

Evan M Anderson 0000-0002-3771-3085
Investigation (equal), Supervision (equal), Writing – original draft (equal), Writing – review & editing (equal)

Lisa N Caravello
Investigation (equal)

Eduardo Garcia
Investigation (equal)

Joseph P Klesko 0000-0003-3989-8009
Investigation (equal), Writing – review & editing (equal)

Samuel D Hawkins 0000-0002-4705-1628
Investigation (equal)

Eric A Shaner 0000-0002-3657-2524
Conceptualization (equal), Formal analysis (equal), Investigation (equal), Supervision (equal), Writing – review & editing (equal)

John F Klem 0000-0002-0598-5780
Conceptualization (equal), Formal analysis (equal), Funding acquisition (lead), Investigation (equal), Project administration (equal), Supervision (equal), Writing – review & editing (equal)

Aaron J Muhowski 0000-0002-5659-6136
Formal analysis (equal), Investigation (equal), Project administration (equal), Supervision (equal), Writing – original draft (equal), Writing – review & editing (equal)

## References

[1] Herbert D J, D'Ascenzo N, Belcari N, Del Guerra A, Morsani F and Saveliev V 2006 Study of SiPM as a potential photodetector for scintillator readout *Nucl. Instrum. Methods Phys. Res.* **567** 356–9

[2] Wagatsuma K, Miwa K, Sakata M, Oda K, Ono H, Kameyama M, Toyohara J and Ishii K 2017 Comparison between new-generation SiPM-based and conventional PMT-based TOF-PET/CT *Phys. Med.* **42** 203–10

[3] Recker M C, Cazalas E J, McClory J W and Bevins J E 2019 Comparison of SiPM and PMT performance using a CLYC scintillator with two optical windows *IEEE Trans. Nucl. Sci.* **66** 1959–65

[4] Seifert S, Van Dam H T, Vinke R, Dendooven P, Lohner H, Beekman F J and Schaart D R 2012 A comprehensive model to predict the timing resolution of SiPM-based scintillation detectors: theory and experimental validation *IEEE Trans. Nucl. Sci.* **59** 190–204

[5] Agishev R, Comerón A, Bach J, Rodriguez A, Sicard M, Riu J and Royo S 2013 Lidar with SiPM: some capabilities and

limitations in real environment *Opt. Laser Technol.*
**49** 86–90

[6] Cervi T *et al* 2018 Comparison between large area PMTs and SiPM arrays deployed in a Liquid Argon Time Projection Chamber at CERN *Nucl. Instrum.Methods phys. Res. Sect. A* **912** 101–4

[7] Hahn A, Mirzoyan R, Dettlaff A, Fink D J, Mazin D and Teshima M 2023 Performance evaluation of three silicon photomultiplier detector modules within the MAGIC telescopes PMT-based camera *Nucl. Instrum. Methods Phys. Res.* **1046** 167686

[8] Liang F and Hoy L 2018 Comparison of NaI coupled to photomultiplier tube and silicon photomultiplier *2018 IEEE Nuclear Science Symp. and Medical Imaging Conf. Proc. (NSS/MIC) 2018 IEEE Nuclear Science Symp. and Medical Imaging Conf. (NSS/MIC)* (IEEE) pp 1–4

[9] Kazkaz K and Swanberg E 2018 *Survey of Current and Future PMT Replacement Technology* (Lawrence Livermore National Lab. (LLNL))

[10] Aitken D W, Beron B L, Yenicay G and Zulliger H R 1967 The fluorescent response of NaI(Tl), CsI(Tl), CsI(Na) and CaF2(Eu) to x-rays and low energy gamma rays *IEEE Trans. Nucl. Sci.* **14** 468–77

[11] Tsao J Y *et al* 2018 Ultrawide-Bandgap Semiconductors: Research Opportunities and Challenges *Adv. Electron. Mater.* **4** 1600501

[12] Vurgaftman I, Meyer J R and Ram-Mohan L R 2001 Band parameters for III–V compound semiconductors and their alloys *J. Appl. Phys.* **89** 5815–75

[13] Masuda T, Tomasulo S, Lang J R and Lee M L 2015 Comparison of single junction AlGaInP and GaInP solar cells grown by molecular beam epitaxy *J. Appl. Phys.* **117** 094504

[14] Prior K A, Davies G J and Heckingbottom R 1984 The thermodynamics of oxygen incorporation into III–V semiconductor compounds and alloys in MBE *J. Crystal Growth* **66** 55–62

[15] Akimoto K, Kamada M, Taira K, Arai M and Watanabe N 1986 Photoluminescence killer center in AlGaAs grown by molecular-beam epitaxy *J. Appl. Phys.* **59** 2833–6

[16] Harmon E S and Hirosky R 2019 Tight pitch compound semiconductor SPAD arrays (Conference Presentation) *Proc. SPIE* **10978** 109780K

[17] Ong J S L, Ng J S, Krysa A B and David J P R 2011 Impact ionization coefficients in Al$_{0.52}$In$_{0.48}$P *IEEE Electron. Device Lett.* **32** 1528–30

[18] Yuan P, Siddiqi N, Zubrod A R, Labios E, Quezada E and Sudharsanan R 2020 High performance InGaP Geiger-mode avalanche photodiodes *Proc. SPIE* **11410** 62–67

[19] Dharmarasu N, Yamaguchi M, Bourgoin J C, Takamoto T, Ohshima T, Itoh H, Imaizumi M and Matsuda S 2002 Majority- and minority-carrier deep level traps in proton-irradiated n+/p-InGaP space solar cells *Appl. Phys. Lett.* **81** 64–66

[20] Lee H S *et al* 2005 Deep-level defects introduced by 1 MeV electron radiation in AlInGaP for multijunction space solar cells *J. Appl. Phys.* **98** 093701

[21] Kim D S, Kim K C, Shin Y C, Kang D H, Kim B J, Kim Y M, Park Y and Kim T G 2006 Defect engineering for 650nm high-power AlGaInP laser diodes *Physica B* **376–377** 610–3

[22] Zaidi M A, Zazoui M and Bourgoin J C 1993 Defects in electron irradiated GaInP *J. Appl. Phys.* **73** 7229–31

[23] Khan A, Yamaguchi M, Bourgoin J C and Takamoto T 2002 Thermal annealing study of 1 MeV electron-irradiation-induced defects in n+p InGaP diodes and solar cells *J. Appl. Phys.* **91** 2391–7

[24] González M, Carlin A M, Dohrman C L, Fitzgerald E A and Ringel S A 2011 Determination of bandgap states in p-type In$_{0.49}$Ga$_{0.51}$P grown on SiGe/Si and GaAs by deep level optical spectroscopy and deep level transient spectroscopy *J. Appl. Phys.* **109** 063709

[25] Chmielewski D J, Jackson C, Boyer J, Lepkowski D, Carlin J A, Arehart A R, Grassman T J and Ringel S A 2017 Comparative study of &>2 eV lattice-matched and metamorphic (AL)GaInP materials and solar cells grown by MOCVD *2017 IEEE 44th Photovoltaic Specialist Conf. (PVSC)* (IEEE) pp 215–8

[26] Cheng C-W, Shiu K-T, Li N, Han S-J, Shi L and Sadana D K 2013 Epitaxial lift-off process for gallium arsenide substrate reuse and flexible electronics *Nat. Commun.* **4** 1577

[27] Brotherton S D 1976 Measurement of deep-level spatial distributions *Solid-State Electron.* **19** 341–2

[28] Armstrong A, Arehart A, Green D, Speck J S, Mishra U K and Ringel S A 2005 A novel method to investigate defect states in MBE grown highly resistive GaN doped with C and Si *Phys. Status Solidi c* **2** 2411–4

[29] Chantre A, Vincent G and Bois D 1981 Deep-level optical spectroscopy in GaAs *Phys. Rev. B* **23** 5335–59

[30] Lucovsky G 1965 On the photoionization of deep impurity centers in semiconductors *Solid State Commun.* **3** 299–302

[31] Pässler R 2004 Photoionization cross-section analysis for a deep trap contributing to current collapse in GaN field-effect transistors *J. Appl. Phys.* **96** 715–22

[32] Grimmeiss H G and Ovren C 1981 Fundamentals of junction measurements in the study of deep energy levels in semiconductors *J. Phys. E: Sci. Instrum.* **14** 1032

[33] Caldas M J, Fazzio A and Zunger A 1984 A universal trend in the binding energies of deep impurities in semiconductors *Appl. Phys. Lett.* **45** 671–3

[34] Reddy P *et al* 2020 Pinning of energy transitions of defects, complexes And Surface States in AlGaN Alloys *Appl. Phys. Lett.* **116** 032102

[35] Walukiewicz W 2001 Intrinsic limitations to the doping of wide-gap semiconductors *Physica B* **302–303** 123–34